A&A 417, 79–91 (2004)
DOI: 10.1051/0004-6361:20034253

Astronomy & Astrophysics

The Galactic Plane region near $\ell = 93°$

II. A stellar wind bubble surrounding SNR 3C 434.1

T. Foster[1,2], D. Routledge[3], and R. Kothes[1,4]

[1] National Research Council of Canada, Herzberg Institute of Astrophysics, Dominion Radio Astrophysical Observatory, PO Box 248, Penticton, BC V2A 6J9 Canada
[2] Dept. of Physics, University of Alberta, Edmonton, Alberta, T6G 2J1 Canada
[3] Dept. of Electrical and Computer Engineering, University of Alberta, Edmonton, Alberta, T6G 2V4 Canada
[4] Dept. of Physics and Astronomy, The University of Calgary, 2500 University Drive NW, Calgary, Alberta, T2N 1N4 Canada

Received 1 September 2003 / Accepted 19 November 2003

Abstract. New Canadian Galactic Plane Survey λ21 cm H I line observations towards supernova remnant (SNR) 3C 434.1 (G94.0+1.0) are presented. We find a fragmented and thin-walled atomic hydrogen shell inside which the SNR is seen to be contained at $v \simeq -80$ km s^{-1}, which we report to be a highly evolved stellar wind bubble (SWB) associated with the remnant. A dark area in the midst of otherwise bright line emission is also seen near -71 km s^{-1}. An absorption profile to the extragalactic continuum source 4C 51.45 (superimposed on the shell's north face) allows us to probe the shell's optical depth, kinetic temperature and expansion velocity. The material in the dark area has the same properties as material in the fragmented shell, suggesting that the dark area is actually the far-side "cap" of the shell seen absorbing emission from warm background gas, the first instance of H I Self Absorption (HISA) seen in such a structure. We show that the kinematic distance of 10 kpc derived from a flat Galactic rotation model is highly improbable, and that this bubble/SNR system is most likely resident in the Perseus Spiral Arm, lying 5.2 kpc distant. We model the SWB shell in three dimensions as a homologously expanding ellipsoid. Physical and dynamical characteristics of the bubble are determined, showing its advanced evolutionary state. Finally, from a photometric search for one or more stars associated with the SWB, we determine that three B0V stars and one O4V star currently inhabit this bubble, and that the progenitor of 3C 434.1 was at latest also an O4 type star.

Key words. ISM: bubbles – ISM: supernova remnants – stars: winds, outflows

1. Introduction

The supernova remnant (SNR) 3C 434.1 ($\ell = 94°$, $b = 1°$) is one of two remnants in the Galactic plane region near $\ell = 94°$, and is seen among a collection of thermal objects. It appears as a radio continuum shell of radius 14 arcmin, smaller than most shell-type remnants visible in the Canadian Galactic Plane Survey (CGPS, Taylor et al. 2003). The 21 cm continuum appearance of this object is similar to the neighboring H II region NRAO 655, discussed by Foster & Routledge (2001, Paper I). The space between these two objects appears filled by dim continuum emission, and the objects appear bridged by this nebulosity. We study the remnant's multi-wavelength appearance in emission and its relationship with NRAO 655 no further here, but in a future publication. In this present paper we report a thorough examination of the neutral material surrounding this SNR, and submit that it is in reality a distant SNR/Stellar Wind Bubble (SWB) pairing.

Send offprint requests to: T. Foster,
e-mail: Tyler.Foster@nrc-cnrc.gc.ca

Stellar winds carve much of the sponge-like structure of neutral hydrogen observed in the interstellar medium. Most of the originators of these winds, including SNR precursors, tend to cluster in associations, and it is thus not surprising to find SNRs evolving into environments greatly modified by groups of massive stars. The legacies of OB star groups are large interstellar cavities, surrounded by expanding outer shells, whose edges are often delineated by swept-up neutral hydrogen, and are thus observable in the H I spectral line. We expect pairings of supernova remnants with H I shells cloaking OB associations to be particularly common within the Galactic spiral arms, where the SNR progenitors and their siblings have formed.

A fine example of a cavity evacuated by an OB cluster and containing an SNR formed within it is seen in the H I environment surrounding the nearby SNR G106.3+2.7 (Kothes et al. 2001). Those authors suggest the formation of the progenitor was triggered by the stellar winds and supernova explosions of cluster members.

We present the discovery of a distant shell of cold atomic hydrogen that surrounds 3C 434.1, and show that it is likely an

old SWB carved out mainly by two O-type stars, one of which was the progenitor of 3C 434.1. The foreground column density is found and hence the distance to the shell and its linear extent, using the new distance technique of Foster & Routledge (2003) (see Sect. 3.3 below). The availability of high-resolution CGPS continuum and H I spectral line data allows observation of the bubble's physical structure, and for the first time neutral material of a stellar wind bubble is seen absorbing emission from warm H I gas behind it. The cold gas of the shell is also seen to absorb emission from the bright and auspiciously located radio continuum point source 4C 51.45, allowing confirmation of parameters and expansion velocity calculated for the shell from emission data. The dynamics and time history of this SWB are modeled and discussed in detail. Finally, from deep *UBV* photometric observations of stars towards 3C 434.1, four stars are identified as candidates for association with the SWB, and the physical effects of this cluster discussed.

2. Observations

2.1. 1420 MHz HI line observations

The field of 3C 434.1 was observed in the 1420 MHz continuum and 21 cm line with the Synthesis Telescope (ST) at the Dominion Radio Astrophysical Observatory (DRAO). The continuum and atomic hydrogen line observations were centred on (ℓ, b) = (93.47°, 1.00°) and are part of the CGPS, a project by a consortium of researchers from five countries to map a large segment of the northern Galactic plane in radio and infrared wavelengths at a resolution approaching 1 arcmin (Taylor et al. 2003). The field of view is 3.1 degrees at 21 cm to the 10% level. The *FWHM* of the beam achieved by the ST is $57'' \times 57'' csc\delta$ in the 1420 MHz continuum. H I line images have 1.1 arcmin resolution in each of 256 channels, and are separated by 0.824 km s^{-1}, with a velocity resolution of 1.3 km s^{-1}. The H I line data have intensity uncertainty due to calibration of ±10%, and the continuum data, ±5%. Other relevant parameters of the telescope and data reduction procedures are given in Sect. 2.1 in Paper I, and further instrumental detail can be found in Landecker et al. (2000).

To depict ISM structures accurately in the CGPS radio continuum and H I line images (especially those of large angular size), missing short-spacing information is routinely added to each ST map. The data are obtained from the Effelsberg 21 cm Galactic Plane Survey (Reich et al. 1997) and an all-sky H I line survey made with the DRAO 25.6m paraboloid (Higgs & Tapping 2000).

2.2. Optical observations

On 2001 August 9, and 2001 November 18, 407 stars in a $27' \times 27'$ field towards $\ell = 94°$, $b = 1°$ (field 1) were observed with the 0.5m optical telescope at the University of Alberta's Devon Astronomical Observatory (Foster et al. 1999). Two separate nights' observations were performed to compare the consistency and assess the final quality of the photometry. A second field (field 2) was also observed (332 stars towards $\ell = 93.70°, b = 1.45°$) for another study, but overlaps some of the SWB interior, and we include the field here. *UBV* filters with optimal passbands for CCDs (as determined by Bessel 1990) were used. The low quantum efficiency of the CCD in the U-band (λ_U = 365 nm) limits the faintest magnitude measured in the sample of stars, and to increase this limit, an average U-band frame was made from nine separate 600 s integrations. Each frame was taken at slightly different altitude (and hence airmass), and we have used the following technique to create a photometrically accurate single frame from many individual ones.

After basic CCD image processing (including removal of cosmic ray strikes and bad pixels), a uniform background level (in analog-digital units, or ADU) for each target frame is determined. This level is subtracted from individual frames. First-order extinction coefficients k'_λ (in units of ADU per unit airmass) for each wavelength are determined from observations of bright northern standard stars (Oja 1996). Stellar fluxes in each frame are then corrected to a common airmass X of zero by multiplying the frame by the factor $10^{k'_\lambda X_{\rm observed}/2.5}$. In this way, the flux is corrected to extra-atmospheric values without affecting the background, which tends to be mostly due to auroral skyglow in our location. Each frame is shifted to a common centre, and a mean image (corrected for atmospheric extinction) is made.

This technique permits accurate photometry to be obtained for very faint stars with modest-sized telescopes: the limiting magnitude for our sample increased to m_V = 16.6, compared to a limiting magnitude of m_V = 14.6 using a single 600 s U-band integration. Nine standard stars from (Oja 1996) were also observed to derive coefficients and zero-point values for transformation of our magnitudes and colours to the Johnson system. Two of these stars (early A-type) were also used as extinction candles, and were observed at varying elevations throughout the night. Extinction and transformation coefficients were very well determined: mean absolute differences between the standard stars' published and measured V, $B-V$, and $U-B$ values are 0.032, 0.018, and 0.036 mag, respectively. As a further check of the quality of our photometry we identified 12 stars in field 1 and 24 stars in field 2, present in the Tycho Catalogue (Høg et al. 2000), as observed by HIPPARCOS. Mean absolute differences between DevonAO and Tycho photometric values (transformed to Johnson's system) were 0.11 mag and 0.13 mag in $B-V$ and V respectively (for field 1), and 0.18 mag and 0.15 mag (field 2).

The $U-B$ versus $B-V$ two-colour diagram was used, along with the reddening curve $E(U-B)/E(B-V) = 0.72+0.05E(B-V)$ and the optical parameter $R_V = A_V/E(B-V) = 3.1$ to derive unreddened colour indices. 93 of the 407 field 1 stars have uniquely determined dereddened colours, as did 83 of the 332 field 2 stars. These are principally O and B-type spectral classes. In determining their unreddened colours and distances, we used the colour index and absolute magnitude M_V calibration of hot stars tabulated in (Cox 2000). Calibration for early-type stars is more certain than for cooler stars (Gathier et al. 1986), and less error in distance is introduced by uncertainties of a star's luminosity class. Nevertheless, one can expect at least ±0.3 mag of uncertainty in M_V for O and early B type stars (Russeil 2003). Luminosity Classes (LC) of the

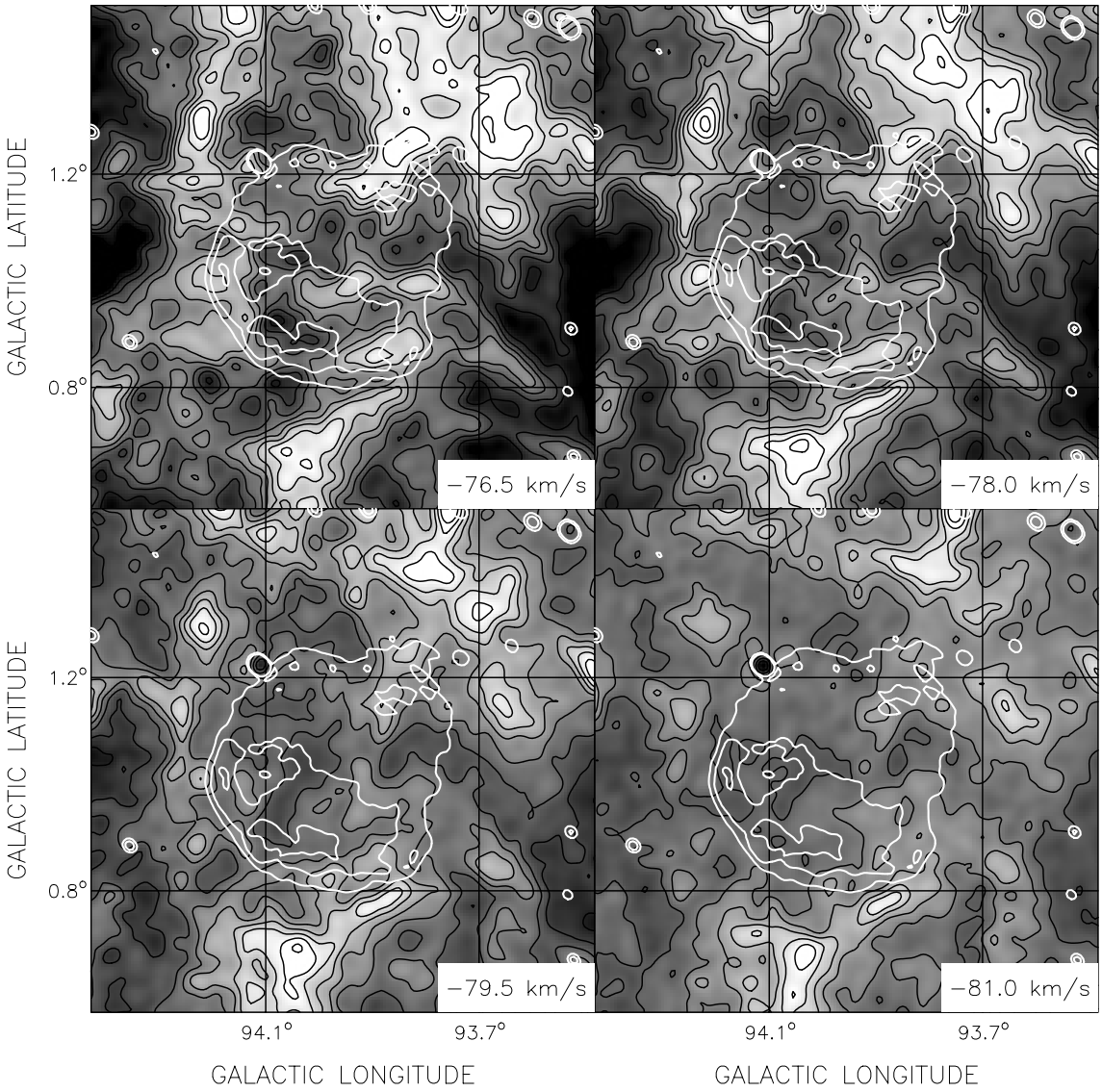

Fig. 1. A montage of H I channel maps, spanning the LOS velocity range $-76.5\ \mathrm{km\,s^{-1}} \geq v \geq -81\ \mathrm{km\,s^{-1}}$. The velocity separation between channels is 1.5 $\mathrm{km\,s^{-1}}$, and the image has been convolved to 2′ resolution. The eastern half of the roughly circular outline of the shell is seen in the first two channels, while the western half outline is seen better in the last two channels. H I contour levels (black lines) for the images are from –20 K to 25 K, incremented in 5 K steps. Greyscale values are from –20 K (black) to +20 K (white), with the average value for each channel subtracted first (from upper left to lower right, 52.9 K, 39.4 K, 27.6 K, and 19.3 K). The 21 cm continuum contour lines of 3C 434.1 (9 K and 12 K) are shown in white.

stars cannot be firmly determined with *UBV* photometry alone, although it is almost certain that the majority are LCV. For the purposes of finding candidate stars for association with the shell around 3C 434.1 (see Sect. 5) we assume all stars are dwarfs.

3. A shell of neutral hydrogen associated with 3C 434.1

In Fig. 1, we present a montage of velocity-channel images of neutral hydrogen towards $\ell = 94°$, $b = 1°$. The angular resolution of each of these maps is 2 arcmin. This H I is visible as a ring of emission surrounding the SNR's radio continuum boundary, in H I channel images between $-76.5\ \mathrm{km\,s^{-1}}$ and $-81.0\ \mathrm{km\,s^{-1}}$, and has the appearance of a fragmented, roughly circular shell, containing the SNR. The ring's mean thickness is 2 arcmin (measured from original 1′ resolution data). The radius of this feature is approximately 21 arcmin, which is 7 arcmin larger than the radius of the continuum shell of 3C 434.1. Figure 2 shows this size relationship well with H I emission summed over three individual channels, centred on $-79.5\ \mathrm{km\,s^{-1}}$.

Figure 2 shows the bubble's perimeter is fairly well defined around most of its eastern half. Its curvature is similar to the SNR's eastern boundary, and the remnant may be interacting with the material of the H I shell in this region. 3C 434.1 is seen as a shell-type SNR in radio continuum, and such emission must be produced by interaction with a dense medium, in this case the inside edge of the H I bubble within which it is evolving. There is fairly good definition in the west edge

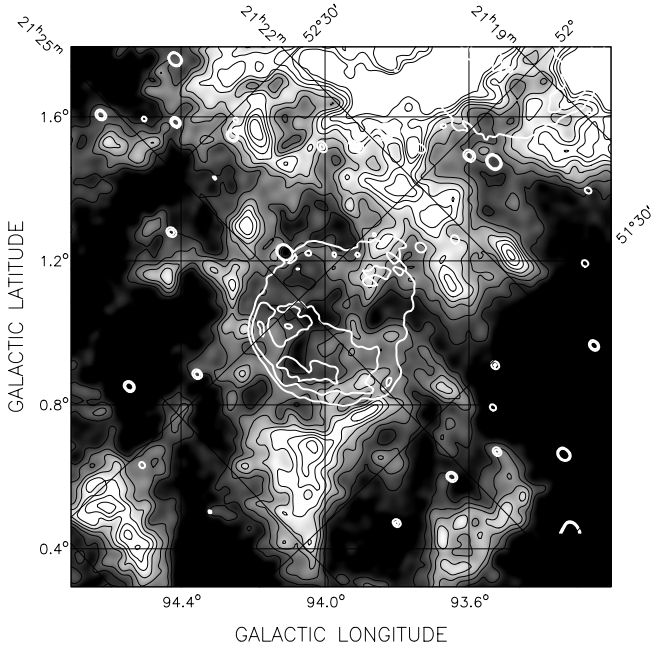

Fig. 2. Average image of three channel maps at half resolution (2′) from -78 km s^{-1} to -81 km s^{-1}, with 21 cm continuum contours of 3C 434.1 overlaid. H I line contour levels are from 24 K to 56 K in 4 K increments, and the greyscale is from 20 K (black) to 40 K (white). Both Galactic and equatorial (J2000) coordinates are shown.

as well especially at -79 km s^{-1} to -81.0 km s^{-1}, though the H I shell edge is similarly fragmented. We show in Sect. 4 that this elliptical ring of H I (see Fig. 3) is most likely material accumulated by an expanding stellar wind bubble (SWB), formed by a cluster of early type stars (including the SNR's progenitor) and inside which 3C 434.1 is evolving.

3.1. Absorption of continuum emission by the H I shell

The radio source 4C 51.45 ($\ell = 94.11°$, $b = 1.23°$) is seen fortuitously projected atop the northern limb of the SNR's continuum boundary (as shown by the contours of continuum emission in Figs. 1 and 2. We find a 21 cm integrated flux density of $S_{1420\ \mathrm{MHz}} = 1.02 \pm 0.06$ Jy. Its peak continuum brightness temperature ($T_{\mathrm{continuum}} = 135$ K) is higher than the mean brightness temperature of neutral hydrogen seen surrounding it and it is absorbed by the H I foreground. This source is projected on the face of the H I shell approximately 7 arcmin south of the north edge. It can be seen to be absorbed out to large negative velocities, suggesting it is extragalactic. For example, the 21 cm H I brightness temperature at the location of 4C 51.45 decreases rapidly, showing that H I absorption is increasing, in the range of velocities shown in Fig. 1. Its unique location allows us to probe the structure of the SWB associated with 3C 434.1.

The optical depth of H I in the line of sight (LOS) towards the north edge of 3C 434.1 is calculated as follows:

$$\tau(v) = -\ln\left(\frac{\Delta T_{\mathrm{line}}(v)}{T_{\mathrm{continuum}}} + 1\right) \quad (1)$$

where $\Delta T_{\mathrm{line}} = T_{\mathrm{on-source}} - T_{\mathrm{off-source}}$ and $T_{\mathrm{continuum}}$ is the continuum brightness temperature of the un-absorbed source (4C 51.45). The H I brightness temperature value $T_{\mathrm{off-source}}$ was calculated in each velocity channel from the mean emission in a 6 arcmin wide annulus (of inner radius 3 arcmin) centred on 4C 51.45, while $T_{\mathrm{on-source}}$ was measured as the peak brightness temperature at the position of source 4C 51.45.

H I emission and absorption ($\Delta T_{\mathrm{line}}(v)$) brightness temperature profiles are shown in Fig. 4, where values of the optical depth (τ) are shown on the right. The extended peak in emission between -35 and -75 km s^{-1} is caused by the Perseus Arm.

We believe the small absorption peaks at -70 km s^{-1} and -96 km s^{-1} are unrelated to large-scale features of Galactic structure, and most likely indicate where the LOS towards 4C 51.45 encounters compressed H I in the back and front edges (respectively) of the aforementioned shell (see Sect. 4.2 below). The absorption peak near -81 km s^{-1} is likely a cold H I cloud which does not show in emission, but is otherwise in the LOS towards 4C 51.45.

In Fig. 5, a dark area is visible through several channels (centred on velocity -71 km s^{-1}), and is superimposed onto the brighter hemisphere of 21 cm synchrotron emission from 3C 434.1. The figure shows that the radius of the dark area enlarges slightly in the first two velocity channels, and is constant thereafter with increasing velocity. This behaviour is what one would expect if the feature were the cap of an expanding bubble. This dark feature does resemble the eastern half of the continuum emission in shape. The mean 21 cm continuum brightness temperature of the SNR's eastern half is 12 K, not enough to be absorbed by H I in foreground channels, so the dark area cannot be the absorbed image of the SNR. However, the resemblance is striking enough to suggest that the SNR shell continuum emission is the result of an interaction with the far inside edge of the H I shell. In the following section, we show that this dark feature is most likely the end cap of the shell, and appears dark because it is absorbing line emission from a warm H I background behind it.

3.2. Self-absorption of background H I emission by the shell

Many small-angular-scale concentrations of cold material in the Perseus Arm are known to have optical depths of 1–2, and absorption of H I emission by cold H I is seen throughout the Perseus Arm. Such H I Self Absorption (HISA, Gibson et al. 2000) is only seen in spectral line images when cold foreground H I has similar velocity to the warm background H I, even though the warm material must be physically displaced (behind) with respect to the cold. Another criterion is that the background H I must be much warmer (and therefore brighter) than the foreground H I.

Figure 4 shows the absorption profile $\Delta T(v) = T_{\mathrm{on}}(v) - T_{\mathrm{off}}(v)$ towards 4C 51.45. Using the optical depth of the shell's near edge ($\tau_{-96} = 0.24 \pm 0.04$), one can find the Boltzmann (spin) temperature of the shell via Eq. (2):

$$T_{\mathrm{spin}} = \frac{T_{\mathrm{shell}}}{(1 - \mathrm{e}^{-\tau})} \quad (2)$$

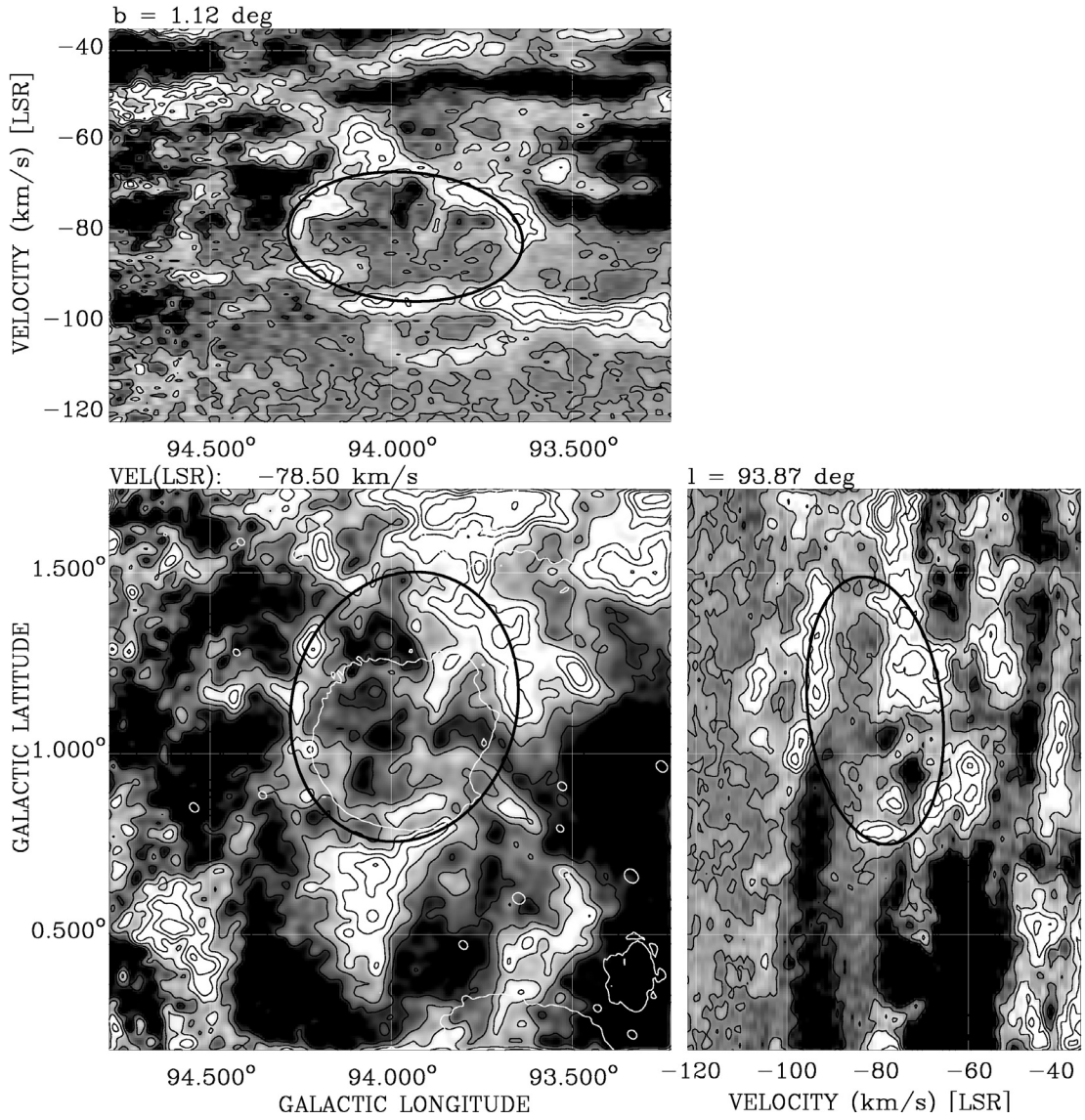

Fig. 3. Three views of the elliptical shell model (thick black ellipses) fitted to the observed H I emission patterns of the shell, in (ℓ, b), (ℓ, v), and (b, v) H I images. The continuum outline of the supernova remnant is shown (white contour).

where $T_{\rm shell}$ is the brightness temperature (above background) of the shell fragments. We find $T_{\rm shell} = 17.3(\pm 14\%)$ K, and $T_{\rm spin} = 80 \pm 16$ K for the ring comprising the shell's edge seen in Fig. 2 (summed channel map at $v = -80$ km s^{-1}).

If the dark area near -71 km s^{-1} in Fig. 5 is to be considered a self-absorbed portion of the SWB shell, two conditions must be met: a) the optical depth of the H I in this far-side cap should be comparable to that measured in the shell's near-side (-96 km s^{-1}), and b) the brightness temperature of the background gas must be much greater than the brightness temperature of gas comprising the shell.

From the brightness temperature of background emission seen at -70 km s^{-1} ($T_{\rm off}(v = -70) = 98.8$ K), and the average value of $\Delta T_{\rm darkfeature} = T_{\rm on-darkfeature} - T_{\rm off}(v = -70) = -27.2$ K found from values of $T_{\rm on-darkfeature}$ measured across the dark feature we find:

$$\tau_{\rm darkfeature} = -\ln\left(\frac{\Delta T_{\rm darkfeature}}{T_{\rm off}(v=-70)} + 1\right) = 0.32 \pm 0.04. \quad (3)$$

The values of optical depth measured for material in the dark feature are therefore similar to those of the shell towards 4C 51.45, and the first condition is met.

We next separate the component of absorption due to a shell (optical depth similar to τ_{-96}) at -70 km s^{-1} from that due to unrelated material at the same velocity by subtracting the absorption peaks ΔT. We find an optical depth of 0.60 ± 0.17 for the remaining material by:

$$\tau = -\ln\left(\frac{\Delta T(v=-70) - \Delta T(v=-96)}{T_{\rm continuum}} + 1\right). \quad (4)$$

This assumes that at the location of 4C 51.45, the shell's far-edge (-70 km s^{-1}) has similar optical depth to that in the near-edge (-96 km s^{-1}). The brightness temperature of the background (in velocity channel -70 km s^{-1}), together with this

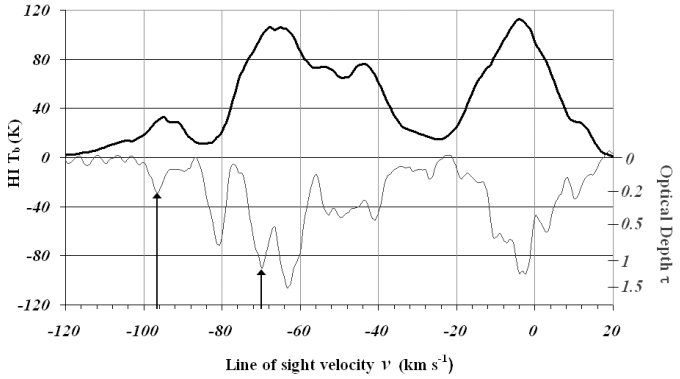

Fig. 4. The average H I emission spectrum (thick black line) towards the SWB surrounding 3C 434.1 is shown, along with the absorption profile $\Delta T = T_{\rm on} - T_{\rm off}$ (thin black line) towards source 4C 51.45 (ℓ = 94.11°, b = 1.23°). The corresponding optical depth τ values are read off the right-hand vertical axis. The absorption peaks from the front (−96 km s^{-1}) and back (−70 km s^{-1}) of the H I shell edges are marked with arrows.

optical depth allows us to calculate the spin temperature of the background gas:

$$T_{\rm background} = \frac{T_{\rm off}(v = -70)}{(1 - {\rm e}^{-\tau})} = 220 \pm 50 \ {\rm K} \qquad (5)$$

which is much greater than the temperature of the shell. Thus, if the dark feature at −72 km s^{-1} is cold material within the SWB shell, the background emission is sufficiently warm to be absorbed by it, and the second condition met. We henceforth will treat this dark feature as the end-cap of the far side of the SWB shell.

3.3. A non-kinematic distance to the SWB

CTB104A and 3C 434.1 are the only supernova remnants known in the Galactic plane vicinity of $\ell = 94°$. Until recently, their distances have been elusive, as have most supernova remnant distances. Uyanıker et al. (2002) kinematically determined the distance to CTB104A (G93.7−0.3) as 1.5 ± 0.2 kpc, a reasonable value considering that the kinematic distance method is probably more valid for local objects than anywhere else (Foster & Routledge 2003). The large line of sight velocity of the SWB associated with 3C 434.1 (∼−79 km s^{-1}) suggests it is very distant: with R_0 = 8.5 kpc and v_0 = 220 km s^{-1}, a kinematic distance of 10 kpc follows. This value can almost certainly be dismissed as inaccurate because of the unreasonable physical parameters indicated for the supernova remnant (e.g. 80 pc diameter). On the basis of the $\sum$-D-z relationship, Mantovani et al. (1982) find a more reasonable range (3.8–6.4 kpc), though this highly disputed method overestimates the distance to CTB104A by nearly a factor of two.

The observed LOS velocity of the SWB surrounding 3C 434.1 is within the velocity range occupied by the Perseus Spiral arm as seen in the H I emission spectrum (see Fig. 6), which crudely suggests that the system is at least as far as the centre of the Perseus arm, likely lying on the Arm's far edge. The large line of sight velocity of the system likely includes contributions from non-circular motions (e.g. the Spiral shock, Roberts 1972), and does not accurately reflect the system's circular velocity from Galactic rotation, causing a severe overestimate of the kinematic distance.

To find a non-kinematic distance to our SNR/SWB system, we apply the new method of Foster & Routledge (2003, hereafter F&R) in the direction ℓ = 94°, b = 1°. The method of F&R begins with a model of the integrated H I column density versus distance $N_{\rm HI}(r)$. After transforming to velocity space (using a velocity-to-distance mapping function $v(r)$ with variable parameters), the model is fitted to the observed cumulative $N_{\rm HI}(v)$ with a χ^2 minimization method. Parameters of both the model $N_{\rm HI}(r)$ and the mapping function $v(r)$ are allowed to vary until an acceptable fit is achieved. The results of this approach are both the model $N_{\rm HI}(r)$ and the function $v(r)$ that together best reproduce the observed distribution $N_{\rm HI}(v)$. The distance to an individual object for which a radial velocity is known is then calculated with either result.

This new technique principally assumes that on a large scale, the observed line of sight velocity (for atomic hydrogen emission) is increasingly negative with distance. For H I in emission and in circular rotation, the assumption that distance is monotonic with velocity is fundamentally true. However, the presence of HISA near −70 km s^{-1} shows that the warm emission throughout the field is physically behind the shell. Thus, when calculating the column density $N_{\rm HI}$ to the SNR/SWB, integrating emission in all channels to the systemic velocity ∼−80 km s^{-1} may overestimate the true foreground column. Conversely, integrating only to an upper limit of v = −70 km s^{-1}; (where the shell begins to appear in velocity space; see Fig. 3) may miss some foreground material appearing at greater negative velocities. We choose our upper limit as an intermediate velocity ∼−75 km s^{-1}, and believe this reasonably estimates the true foreground column density.

We thus integrate H I emission (shown in Fig. 6) alone to this velocity, and find the foreground H I column density to 3C 434.1 to be $N_{\rm HI} = (1.04 \pm 0.10) \times 10^{22}$ cm^{-2}. To the Galactic edge, we find $N_{\rm HI}(r = \infty) = (1.18 \pm 0.11) \times 10^{22}$ cm^{-2}. The distance to the SNR/SWB that corresponds with $N_{\rm HI}$ is 5.2 ± 1.1 kpc. Figure 6 shows this distance predicted by the method's output of cumulative column density as functions of distance and velocity for this direction. Most of the distance uncertainty derives from uncertainties in $N_{\rm HI}$ and $N_{\rm HI}(r = \infty)$.

4. Kinematic model of the expanding SWB

In the (ℓ, b) image in Fig. 3, a ring of H I emission is visible surrounding the SNR. This image shows the H I emission summed over four channels centred on −78.5 km s^{-1}. The H I ring has the appearance of a fragmented shell, possibly an expanding SWB surrounding the SNR. We searched for the corresponding elliptical "cross sections" of such an expanding shell in longitude-velocity and latitude-velocity images, and the results are shown in the (ℓ, v) and (b, v) plots in Fig. 3, respectively.

4.1. The expanding SWB observed in HI emission

The (ℓ, b), (ℓ, v), and (b, v) H I emission patterns seen in Fig. 3 are crudely compatible with a spherical H I shell of radius ≃21′

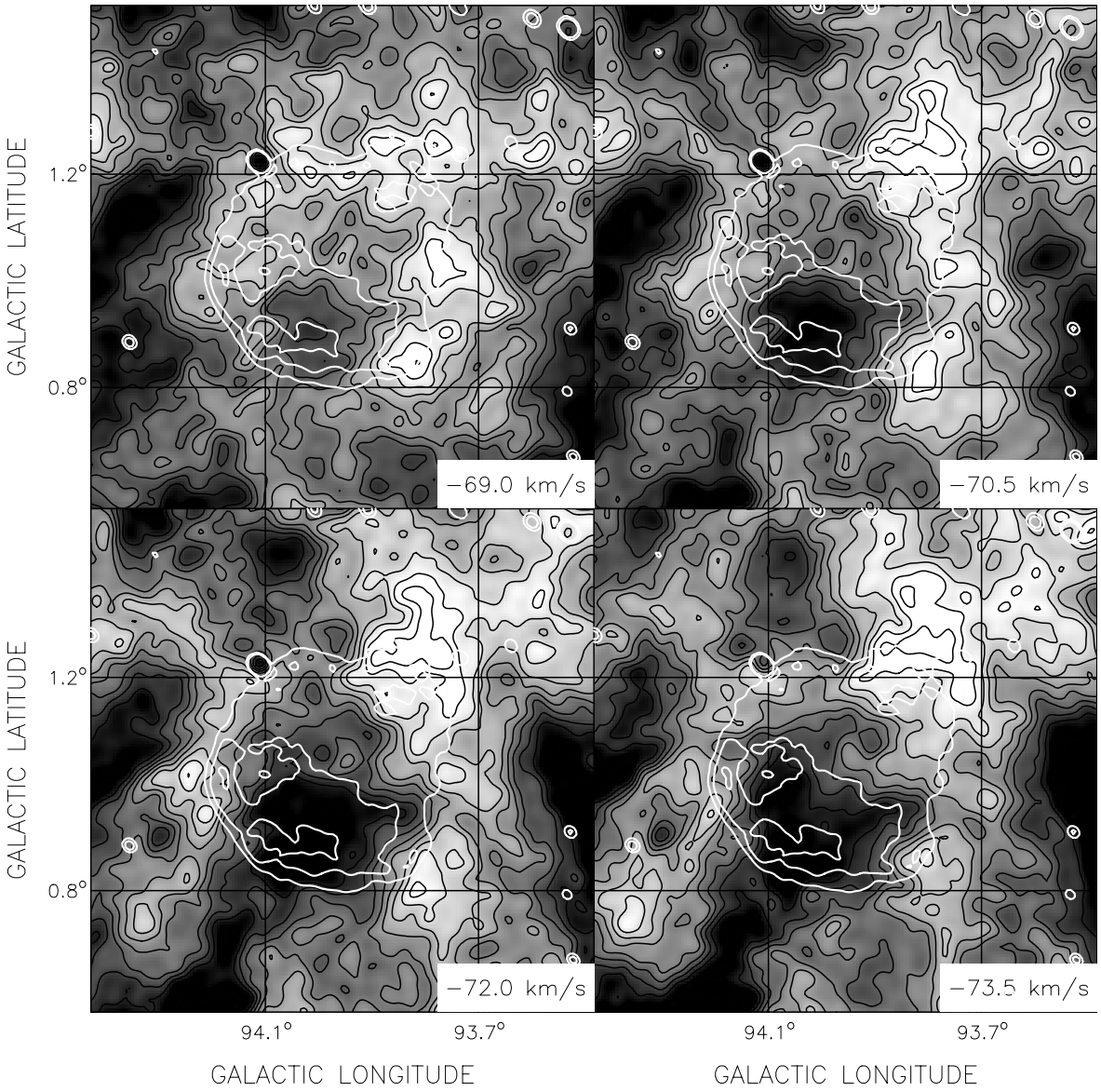

Fig. 5. A montage of H I channel maps, spanning velocities $-69.0\ \mathrm{km\,s^{-1}} \geq v \geq -73.5\ \mathrm{km\,s^{-1}}$, showing the dark area (centred on $\ell = 94°$, $b = 0.9°$) described in Sects. 3.1 and 3.2. Resolution and channel separation are the same as in Fig. 1. The dark area appears within a generally uniform warm H I background, and is likely cold end-cap material of the shell absorbing this background emission. Contour levels and greyscale are the same as Fig. 1, with the following average values subtracted: 96.5 K, 92.2 K, 85.4 K, and 76.9 K.

centred on $(\ell, b) \simeq (93.97°, 1.10°)$, having a systemic velocity $v_{\rm sys} \simeq -80\ \mathrm{km\,s^{-1}}$, and a radial expansion velocity given by half its extent in velocity, i.e. $v_{\rm e} \simeq 13\ \mathrm{km\,s^{-1}}$. However, the (ℓ, b) outline of the H I shell is actually elliptical, and the (ℓ, v) outline is also slightly skewed. This suggests that rather than being spherical, the expanding H I shell may in fact be *ellipsoidal*, and that the ellipsoid is inclined with respect to our line of sight.

A simple kinematic model for an expanding ellipsoid was constructed for the H I shell. The objective of creating the model was to reproduce the appearance of the (ℓ, b), (ℓ, v), and (b, v) "sections" through the ellipsoidal shell which are recognizable in Fig. 3. To minimize the number of free parameters, the ellipsoid was allowed only two parameters of size: a semi-major axis a_1 and a semiminor axis a_2. The ellipsoid is assumed to have a circular cross-section; the nomenclature implies that it is prolate, though it could equally well be oblate. The major axis can be rotated in yaw (ϕ) and pitch (ψ) as shown in Fig. 7. The observer is located on the z-axis; hence Galactic coordinates ℓ and b correspond to $-x$ and y, respectively. As shown, positive ϕ yaws the ellipsoid's major axis counterclockwise as seen from above, while positive ψ pitches the end of its major axis upwards which is closest to the observer.

In the kinematic model, a shell of one voxel thickness is created which occupies all voxels satisfying

$$\frac{x'^2}{a_2^2} + \frac{y'^2}{a_2^2} + \frac{z'^2}{a_1^2} = 1. \tag{6}$$

The ellipsoid is oriented relative to the observer through the relations:

$$x = x' \cos\phi + 0 + z' \sin\phi = b_{11}x' + b_{12}y' + b_{13}z' \tag{7}$$

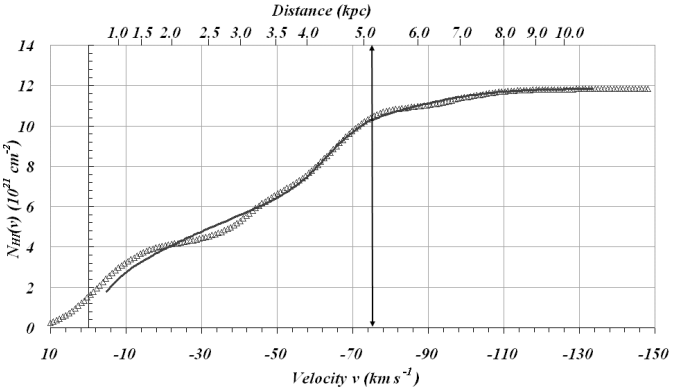

Fig. 6. The observed cumulative column density-velocity relation $N_{\rm HI}(v)$ (open triangles) towards $\ell = 94°$, $b = 1°$. The fitted model $N_{\rm HI}(v)$ is also shown (solid line). The distance-velocity relation $v(r)$ that results from the fit is used to determine the corresponding heliocentric distance (plotted on the top horizontal axis). The integration limit velocity (-75 km s^{-1}) to which we believe all H I emission between the SWB/SNR and the Sun is foreground is shown with an arrow. The SWB/SNR distance predicted by the fitted model $N_{\rm HI}(v(r))$ is $d = 5.2 \pm 1.1$ kpc.

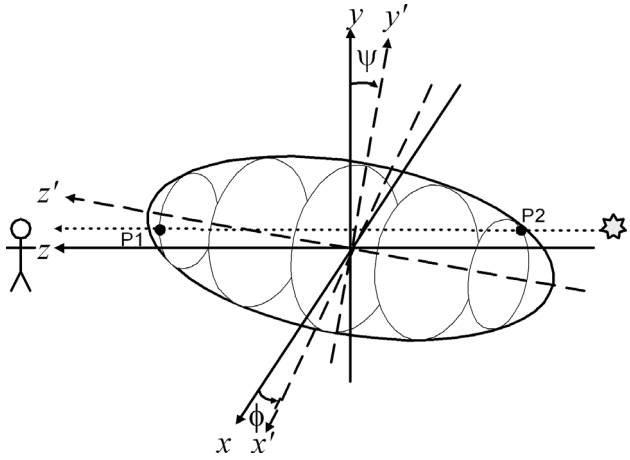

Fig. 7. Sketch of the model H I shell's orientation and geometry, showing the viewing angles ϕ and ψ (defined in Sect. 4.1) and points of intersection (P1, P2) between the shell and the LOS towards background continuum source 4C 51.45 (shown by the star symbol). The ellipticity of the model is exaggerated.

$$y = x' \sin\phi \sin\psi + y' \cos\psi - z' \cos\phi \sin\psi \quad (8)$$
$$= b_{21}x' + b_{22}y' + b_{23}z'$$

$$z = -x' \sin\phi \cos\psi + y' \sin\psi + z' \cos\phi \cos\psi$$
$$= b_{31}x' + b_{32}y' + b_{33}z'. \quad (9)$$

For simplicity, each voxel of the shell is assigned an expansion velocity directed radially outward from the origin of the ellipsoid, with the magnitude of the expansion velocity assumed to be proportional to the radial displacement of the voxel from the origin of the ellipsoid. Such a proportionality is a property of any power-law expansion. That is, the ellipsoidal shell is imagined to be expanding homologously so that its shape stays constant as it expands. The line-of-sight velocity of any voxel in such a shell is simply the radial expansion velocity of that voxel, projected onto the z-axis, if the shell as a whole has zero systemic velocity. We define $v_{\rm sys}$ as the systemic line-of-sight velocity of the origin of the ellipsoid. The z-axis points toward the observer, as shown in Fig. 7, but astronomical convention is that positive velocities are directed *away* from the observer; hence the line-of-sight velocities must be negated to conform to convention.

To create a (b, v) plot, all voxels can be found in which a plane at $x = 0$ intersects the tilted ellipsoid, with the z-coordinate of each such voxel (the component of its radius vector projected onto the z-axis) being proportional to the LOS expansion velocity of that voxel, relative to $v_{\rm sys}$. For a power-law expansion $R(t) = R_{\rm initial}t^n$, for example, the proportionality relation between radial position of a voxel and its radial expansion velocity is $R(t) = t/n \times {\rm d}R/{\rm d}t = t/n \times v_{\rm e}(t)$ for any expansion age t.

Similarly, to create an (ℓ, v) plot, a plane at $y = 0$ intersects the tilted ellipsoid. To permit the (b, v) and (ℓ, v) "sections" through the ellipsoid to be taken at ℓ and b positions which do not coincide with the origin, however, fixed offsets in x and y respectively are permitted. Thus in the (b, v) plot in Fig. 3, $\ell = 93.87°$, and in the (ℓ, v) plot $b = 1.12°$, whereas the origin of the ellipsoid is taken as $(\ell_0, b_0) = (93.961°, 1.123°)$.

In a similar manner, in constructing an (ℓ, b) plot a plane at $z = 0$ can intersect the tilted ellipsoid. To allow the line-of-sight velocity chosen for the (ℓ, b) plot to differ from $v_{\rm sys}$ of the ellipsoid, a fixed offset in z is permitted, corresponding to sliding this plane, which is orthogonal to the line of sight, toward or away from the observer along the z-axis. Thus in Fig. 3, the (ℓ, b) "section" is at $v = -78.5$ km s^{-1}, whereas $v_{\rm sys}$ for this modelling process is set to -82 km s^{-1}, corresponding to an offset in z of 7 pc away from the observer using the relation $R = tv/n$ above. The parameters chosen for the model ellipsoid whose "sections" are drawn in Fig. 3 are $a_1 = 36$ pc, $a_2 = 29$ pc, $\phi = 35°$, $\psi = 70°$, and $v_{\rm sys} = -82$ km s^{-1}. The distance is assumed to be 5.2 kpc, the origin is taken as $(\ell_0, b_0) = (93.961°, 1.123°)$, the exponent n in $R(t) = R_{\rm initial}t^n$ is assumed to be 3/5, and the age t of the expansion is $\sim$1.2 Myr. While likely not unique, this set of parameters reproduces the H I *emission* appearance of the shell reasonably well in (ℓ, b), (ℓ, v), and (b, v), as shown in Fig. 3.

We are very fortunate in the case of the SWB surrounding 3C 434.1, to find a strong extragalactic continuum source, 4C 51.45, on the same line of sight. The line-of-sight velocities at which H I *absorption* of this source is produced by the shell of the SWB can now be used to check the parameters for the expanding ellipsoid found above using only H I in emission.

4.2. The expanding SWB observed in HI absorption

The expanding ellipsoidal shell model introduced in Sect. 4.1 above is useful for interpreting H I absorption spectra as well as for producing (ℓ, b), (ℓ, v), and (b, v) "sections" of an H I shell seen in emission. For an absorption spectrum, given the position $(\ell_{\rm source}, b_{\rm source})$ of a background continuum source relative to the origin (ℓ_0, b_0) of the ellipsoidal shell, the points P1, P2 in Fig. 7 can be found at which the line of sight to the source

intersects the ellipsoidal shell. Then the corresponding line-of-sight velocities follow from the z-coordinates of P1, P2 under the assumption that the expansion velocity of any voxel in the shell is proportional to its distance from the origin, as stated earlier. Using $x = -(\ell_{\rm source} - \ell_0)$ and $y = (b_{\rm source} - b_0)$ we find:

$$z_{1,2} = b_{31}x' + b_{32}y' + b_{33}z' \tag{10}$$

where

$$x' = \frac{1}{2a}\left(-b \pm \sqrt{b^2 - 4ac}\right) \tag{11}$$

$$y' = \left(\frac{b_{11}b_{23}}{b_{13}b_{22}} - \frac{b_{21}}{b_{22}}\right)x' + \left(\frac{y}{b_{22}} - \frac{b_{23}x}{b_{13}b_{22}}\right) \tag{12}$$

$$z' = \frac{x - b_{11}x'}{b_{13}} \tag{13}$$

and

$$a = \frac{b_{11}^2 a_2^2}{b_{13}^2 a_1^2} + 1 + \left(\frac{b_{11}b_{23}}{b_{22}b_{13}} - \frac{b_{21}}{b_{22}}\right)^2 \tag{14}$$

$$b = 2\left(\frac{b_{11}b_{23}}{b_{13}b_{22}} - \frac{b_{21}}{b_{22}}\right)\left(\frac{y}{b_{22}} - \frac{b_{23}x}{b_{13}b_{22}}\right) - \frac{2a_2^2 b_{11}x}{a_1^2 b_{13}^2} \tag{15}$$

$$c = \left(\frac{y}{b_{22}} - \frac{b_{23}x}{b_{13}b_{22}}\right)^2 - a_2^2 + \frac{a_2^2 x^2}{a_1^2 b_{13}^2} \tag{16}$$

with all quantities in the same units (e.g. pixels). Then the line-of-sight velocity of the voxel at P1 or P2 equals the radial expansion velocity of that voxel, projected onto the z-axis, negated to conform to convention, and added to $v_{\rm sys}$ of the ellipsoid:

$$v_{1,2} = v_{\rm sys} - \frac{nz_{1,2}}{t} \tag{17}$$

in which we draw on the relation $R = tv/n$ as before.

Since 4C 41.45 is located at $(\ell_{\rm source}, b_{\rm source}) = (94.11°, 1.22°)$ whereas the origin of the ellipsoid is set to be $(\ell_0, b_0) = (93.961°, 1.123°)$, we enter $x = 8.9'$ (25 pixels) and $y = 5.8'$ (16 pixels) in the foregoing. Using the parameters for the SWB deduced in Sect. 1.1 from the (ℓ, b), (ℓ, v), and (b, v) H I *emission* patterns, the expressions above predict that H I absorption occurring in the ellipsoidal shell should appear at line-of-sight velocities of -93.8 km s^{-1} and -70.1 km s^{-1}.

Figure 4 shows the observed H I absorption profile towards 4C 51.45, and in it we see a weak absorption peak near -96 km s^{-1} and another peak near -70 km s^{-1}. Thus the absorption features seen in the 4C 51.45 H I *absorption* profile do substantiate the values found for the SWB parameters in the previous H I *emission* analysis. An important physical result from this kinematic analysis is the expansion velocity (along the degenerate minor axes of the ellipsoid): $na_2/t \sim 14$ km s^{-1}.

Table 1. Observed and calculated physical and dynamical characteristics of the ellipsoidal stellar wind bubble surrounding 3C 434.1.

Parameter	Value
Geometric Centre (ℓ_0, b_0)	93.961°, 1.123°
Systemic velocity $v_{\rm sys}$	-79 km s^{-1}
Distance	5.2 ± 1.1 kpc
Size (semimajor, semiminor axes)	36 ± 7 pc, 29 ± 6 pc
Mean Thickness of Shell	3.1 ± 0.6 pc
Expansion Velocity $v_{\rm e}$	14 ± 3 km s^{-1}
H I density within shell n	12.9 ± 2 cm^{-3}
Local ISM H I density n_0	4.6 ± 1 cm^{-3}
H I mass within shell $M_{\rm shell}$	$14\,500 \pm 2500\ M_\odot$
Kinetic energy of shell $E_{\rm k}$	$2.8 \pm 0.5 \times 10^{49}$ ergs

4.3. Physical characteristics and dynamical considerations

The differential column density of the shell wall measured at the position of 4C 51.45, and adjusted for path length is:

$$\Delta N_{\rm HI} = 1.823 \times 10^{18} \frac{T_{\rm shell}}{1 - {\rm e}^{-\tau}} \tau \Delta v \times \sin\theta \cos\phi \tag{18}$$

where $T_{\rm shell}$ is the brightness temperature (above background) of the shell (from Sect. 3.2, 17.3 K), and θ (50°) and ϕ (9.6°) are the angular locations (in spherical polar coordinates) of the 4C 51.45 absorption feature on the surface of the shell, assumed a sphere for this estimate. Integrating across the velocity width of the τ-line centred on -96 km s^{-1} (see Fig. 4), we find $\Delta N_{\rm HI} \simeq 1.2 \times 10^{20}$ cm^{-2}. This is taken as representative of the typical column density through the shell normal to its surface. Assuming a uniform thickness of $2'$ and the elliptical shape for the shell modelled in the previous section, the mean density of swept-up neutral hydrogen within the shell is $n_{\rm HI} \sim 13$ cm^{-3}. We thus infer that the environment into which the bubble expanded had an original ambient density of $n_0 \sim 5$ cm^{-3}, a typical value for the interstellar medium within a spiral arm undisturbed by massive stars. The mass of material swept up in the shell is $14\,500\ M_\odot$, (accounting for 9% helium abundance by number in the surroundings), and the kinetic energy of the shell $E_{\rm k} = 2.8 \times 10^{49}$ erg. Table 1 lists these and other physical characteristics of the shell. The observed size and expansion rate of our H I bubble suggests it has certainly evolved beyond the first stage of bubble evolution (free expansion), and is likely well into the second, longest-lasting phase of evolution (the energy-driven phase) where the formation of a thin cold outer shell is expected due to minor radiative losses at the shell periphery.

The following equation governs the evolution of a typical energy-conserving interstellar bubble (Eq. (51), Weaver et al. 1977) with no losses:

$$R(t) = 27 n_0^{-\frac{1}{5}} L_{36}^{\frac{1}{5}} t_6^{\frac{3}{5}} ({\rm pc}), \tag{19}$$

where n_0 is the ambient interstellar density, L_{36} is the power of the stellar wind ($L_{\rm w}$) responsible for the shell's formation (in units of 10^{36} erg s^{-1}), and t_6 is the time (10^6 yr). Accounting for radiative loss produces an analytically intractable equation. Weaver et al. (1977) numerically simulate the evolution of a bubble accounting for radiative loss, and find that $R(t)$

evolves as a power law with exponent 0.58, intermediate between Eq. (19) and the law $R(t) \propto \sqrt{t}$ of Steigman et al. (1975). Koo & McKee (1992) find a similar solution for a partially radiative bubble, for which the shell radius will expand with a power law of index 4/7. One can see that partial radiative losses affect the time evolution of a bubble in only a small way. Therefore, in estimating parameters for our SWB, we retain the use of Weaver et al.'s analytic evolutionary equation (Eq. (19)) for the analysis. The dynamical age of the bubble is calculable by combining $R(t)$ with its first derivative: $t \approx 0.6R/v_e$. With $R = 34$ pc and $v_e = 14$ km s^{-1} we find $t \sim 1.4 \times 10^6$ yr, agreeing reasonably well with the estimate of 1.2 Myr from Sect. 4.1.

We assume the SWB was created by the progenitor and other O and B stars of the same cluster, and therefore the age of the SWB must be at least equal to the main-sequence lifetime of the progenitor star (assuming the age of the SNR itself is negligible). Since there is no massive star with such a short lifetime (1.4 Myr), an apparent conflict exists between the dynamical age of the bubble and the age of the SNR progenitor. Conflicts between kinematic and evolutionary ages of stellar wind bubbles have been observed by numerous authors (e.g. Cazzolato & Pineault 2003; Cappa et al. 2002) and the puzzle is highlighted in the review of Garmany (1994), who states the discrepancy is often by a factor of 2. This is similar to the uncertainty that lies within the non-radiative stellar wind bubble solutions of Weaver et al. (1977). Explanations such as non-coeval star formation have been proposed (Saken et al. 1992), but cannot be proven here. We must believe that the true age of our system is likely much greater than 1.4 Myr, possibly up to 2.8 Myr. A plausible age nearer to this upper limit is supported by the discovery of an O4V type star within our bubble (see Sect. 5). The main-sequence lifetime given by Chiosi et al. (1978):

$$t_* = 4.4 \times 10^6 (S_{49})^{-\frac{1}{4}} (\mathrm{yr}) \quad (20)$$

is 2.6 Myr, where $S_{49} = 8.5$ is the rate at which an O4V star emits ionizing photons (S), in units of 10^{49} s^{-1} (Panagia 1973). This lifetime is for an intermediate mass O4V star, or about 70 $M_\odot$ in Schaerer & de Koter (1997), who show evolutionary models for O4V stars from 60 $M_\odot$ (3.4 Myr) to 85 $M_\odot$ (1.7 Myr).

Simultaneously in solving for the SWB age t, we solve for the wind luminosity of the enclosed star(s). At the minimum age of the system (1.4 Myr), $L_w \sim 5.1 \times 10^{36}$ erg s^{-1}, and at the maximum (2.6 Myr), $L_w \sim 8.4 \times 10^{35}$ erg s^{-1}. Assuming a constant wind luminosity over the bubble's minimum lifetime, the energy imparted to the SWB's expansion is $\epsilon = E_k/E_w = 0.12$ times the total energy output ($E_w = 2.3 \times 10^{50}$ ergs). This efficiency is 0.07 if the bubble is considered as old as the 2.6 Myr main sequence lifetime of the O star we find within it.

4.4. Energy considerations

The wind luminosity of a star powering the SWB is related to the terminal wind velocity v_w and mass-loss rate ($\dot{M}_6 = \dot{M}/10^{-6}\ M_\odot\ \mathrm{yr}^{-1}$) as $\dot{M}_6 v_{2000}^2 \approx 1.26 \times L_{36}$ (where we define $v_{2000} = v_w/2000$ km s^{-1}). From the above wind luminosity one calculates $\dot{M}_6 v_{2000}^2 \simeq 6.4$. Following McKee et al. (1984), the *characteristic* wind luminosity for a bubble formed in a medium with density n_0 is:

$$L_{st} = 1.26 \times 10^{36} \left(S_{49}^2/n_0\right)^{1/3} (\mathrm{erg\ s^{-1}}). \quad (21)$$

Main sequence stars from O4−O8 typically produce $S_{49} = L_{36}^{2/3}$ (±20%) photons per second (Abbot 1982; Panagia 1973), and if the star(s) that formed our SWB are similar, then $S_{49} = 3$. McKee et al. (1984) also define the dimensionless wind luminosity $L_w^* = L_w/L_{st}$ as a gauge of the relative strength of the outflow. The minimum age of the bubble (1.4 Myr) gives $L_w^* = 3.26$, while at the bubble's plausible age of 2.6 Myr, we find $L_w^* = 0.5$ indicating a weak outflow, and that the wind-blown cold H I shell is likely filled with the hot wind of the resident stars. Thus cool shell material is evaporating and mixing with the internal hot wind, reducing the pressure caused by the wind and slowing the shell's expansion. It is probable that the H I shell's expansion has slowed due in part to such cooling, and its exterior is beginning to fragment, consistent with its current appearance.

Using the equations of McKee et al. (1984) we have calculated a simple time history model of a SWB blown by a single star, into a medium with $n_0 = 5$ cm^{-3}. A single O5.5V star is used, as the wind luminosity of such a star ($L_{36} = 3.5$) is the closest match to the wind luminosity of the bubble found in Sect. 4.3 at its minimum age ($L_{36} = 5.1$). In our model, the O5.5V star's *entire* mechanical energy output contributes to the formation of the bubble, whereas in reality the energy conversion efficiency is 20% or less (Koo & McKee 1992). The characteristic wind luminosity of the system at time $t = 0$ is $L_w^* = 2.73$, closely matching the value calculated for our bubble at its minimum age ($L_w^* = 3.26$). The radius, velocity and age are found at which the bubble stalls, and are where pressure between the bubble's interior is balanced by the confinement pressure of the photoionized hydrogen surrounding the bubble. The bubble also becomes radiative at this point. Table 2 shows that the model bubble stalls when it reaches $t = 2.6$ Myr, at a radius of 50 (±10) pc, within the uncertainty of our elliptical model's

Table 2. Comparison of observed SWB parameters to those calculated from a simple time-evolution model of a SWB formed by the wind of a single O5.5V star, chosen to match the observed wind luminosity L_w at the minimum age of the bubble ($t = 1.4$ Myr). Model is from McKee et al. (1984). The stall velocity and age for the bubble are near the lower and upper limits of those same parameters as measured, respectively. The stall radius is 30% larger than the observed radius, but is within uncertainties. The SWB surrounding 3C 434.1 is apparently in its early stages of dissipation.

Parameter	Model	Observed
$L_w(10^{36}$ erg s$^{-1})$	3.5	5.1
L_w^*	2.73 (at $t = 0$)	3.26 (at $t = 1.4$ Myr)
$S_{49}(10^{49}$ photons s$^{-1})$	2.3	3.0
Stall Radius R_b (pc)	50 ± 10	34 ± 7
v_e at stall (km s^{-1})	11.4 ± 2.3	14
t_{stall} (10^6 yr)	2.6 ± 0.5	1.4–2.6

mean radius (34 ± 7 pc). The stall velocity of 11.4 km s^{-1} is very nearly that calculated for the ellipsoidal model (14 km s^{-1} in Sect. 4.2). Considering the fragmented appearance we observe our SWB to have, the above simple model suggests that it is certainly highly evolved, and has certainly reached the last stages of Phase II. The rate of expansion due to momentum conservation has slowed to nearly the sound speed of the unperturbed medium, and the SWB's dissipation in the ISM has begun. For a "standard" bubble ($n_0 = 1$ cm^{-3}, $L_{36} = 1.3$, Weaver et al. 1977) the dissipation time is approximately given by the main-sequence lifetime of the star, in this case 2.6×10^6 yr. We are thus likely viewing the last period of this bubble's identity within the ISM.

5. Stellar residents within the SWB

We have carried out a search towards the direction of the SWB for O and B-type stars that could be associated with the SWB, and we here present the results of this search.

An observational bias of overweighting luminous objects will afflict a magnitude-limited sample of stars, especially out to great distances. This Malmquist bias will affect our observations, which therefore will reveal only the most massive and brightest stars at the distance of the SNR/SWB (5.2 kpc). This bias is pushed further towards luminous stars by the large total extinction A_V suffered by radiation (see below). On the other hand, the patchiness of interstellar extinction (Boyle et al. 1992, the effects of which have been found on scales down to 30 square arcmin by) makes it likely that many stars within our 730 square arcmin fields will be observed through transparent "windows" in the dust column (or conversely through dust screens). These effects, coupled with uncertainties in absolute magnitude M_V calibration (at least ±0.3 mag, or 15% distance uncertainty) mean that a wide range of stars could be considered as possible candidates for association with the SWB. We quantify the selection criteria as follows.

First, we estimate the mean extinction to the SWB by measuring the hydrogen column density in the foreground. We express this column in visual magnitudes using the gas to dust ratio of Predehl & Schmitt (1995), $N_{\rm H}/A_V = 1.79 \pm 0.03 \times 10^{21}$ cm^{-2} mag^{-1}. From H I in emission, the column density from Sect. 3.3 amounts to 6 mag of extinction. This is likely a lower limit as H I within the entire column may not all be optically thin, a fact illustrated by the higher extinction found using the absorption profile towards 4C 51.45, which shows an H I column amounting to at least 7 mag of foreground extinction. This optically thick H I may not be uniformly distributed over the observed field and distance column, so a mean extinction of 6.5 mag to the SNR/SWB is adopted, equivalent to a reddening of $E(B-V) \sim 2.1$ mag. We conservatively estimate the variation in $E(B-V)$ across the observed field 1 by calculating the standard deviation $\sigma_{E(B-V)}$ of reddenings for all stars in distance bins 250 pc wide, out to 2.5 kpc. A total reddening scatter of $\sigma_{E(B-V)} \approx 0.42$ mag is calculated in this manner. Since our photometric error is small (see Sect. 2.2), this scatter is likely due to the irregular distribution of local dust across the field.

Thus stars for which $E(B-V)$ falls within 2.1 ± 0.4 mag, and distance d within 5.2 ± 1.0 kpc are considered candidates. For the given extinction ($A_V = 6.5 \pm 1.2$ mag) and distance, the expected minimum stellar type that could be detected in our magnitude-limited sample ($m_V = 16.6$ mag) is B1V ($M_V = -3.2$ mag). At the edge of the uncertainties, we may find stars down to B2.5V ($M_V = -2.0$ mag).

Of the 100 or so classified O and B stars seen towards the interior of the SWB, only 12 have reddenings $E(B-V) \approx 1.7$ mag or greater. If we assume all are main sequence stars, then eleven remain for which $d \leq 5.2 \pm 1.1$ kpc. Table 3 lists the characteristics of these stars, and shows their photometric distances (assuming a common luminosity class of V). Three B0V stars have distances and reddenings that are very consistent with the SWB: Stars 1, 4, and 10 are the most likely residents. The O4-type Star 7 also has a very consistent distance and reddening. Much less certain and barely within the distance uncertainties is Star 2 and other stars fall short of being solid candidates. We can comfortably conclude that only Stars 1, 4, 7 and 10 are candidates for association with the SWB surrounding 3C 434.1. Figure 8 shows the positions of these stars (circled) within the SWB, and with respect to the radio continuum appearance of 3C 434.1. The wind-dominant O4V star is found very nearly in the centre of the bubble. There are no stars in field 2 that match the selection criteria.

We now consider whether the observed wind luminosity and energy requirements of the bubble are met by the winds of the observed candidate stars. For our analysis, we use terminal wind velocities and mass loss rates from the models of Schaerer & de Koter (1997). The adopted parameters are listed in Table 4, and it is seen that the integrated wind luminosity of the observed stars is $\dot{M}_6 v_{2000}^2 = 3.7$, accounting for ~50% of the wind luminosity sustaining the bubble at age 1.4 Myr ($\dot{M}_6 v_{2000}^2 = 6.4$). This is predominantly from the O4V star.

That there are no other stars observed within this SWB with outputs significant enough to affect the bubble's evolution is likely, considering that B0V stars are the latest type observed here, and these are seen in Table 4 to have an almost negligible contribution to the wind luminosity $\dot{M}_6 v_{2000}^2$. The missing wind luminosity gives us an estimate of the latest stellar type for the progenitor of SNR 3C 434.1. Another O4V star would bring the total internal wind luminosity up to $\dot{M}_6 v_{2000}^2 = 6.8$, and such a star has a main-sequence lifetime consistent with the upper-limit estimate of the bubble's age (2.6 Myr). The progenitor may even have been of an earlier spectral type than this, but should not have been much cooler, as such a star would have outlived the currently observed O4V star within the bubble. This suggests it is probable that SNR 3C 434.1 marks the first supernova event to occur within this bubble, and the explosion was of type Ib or Ic.

Figure 8 shows that there is 30% (by area) of the SWB's interior not covered in the optical observations. It is very unlikely that other powerful stars related to the SWB lurk in these peripheral unobserved regions, as their winds would have certainly distorted the elliptical outline of the bubble (see Fig. 3).

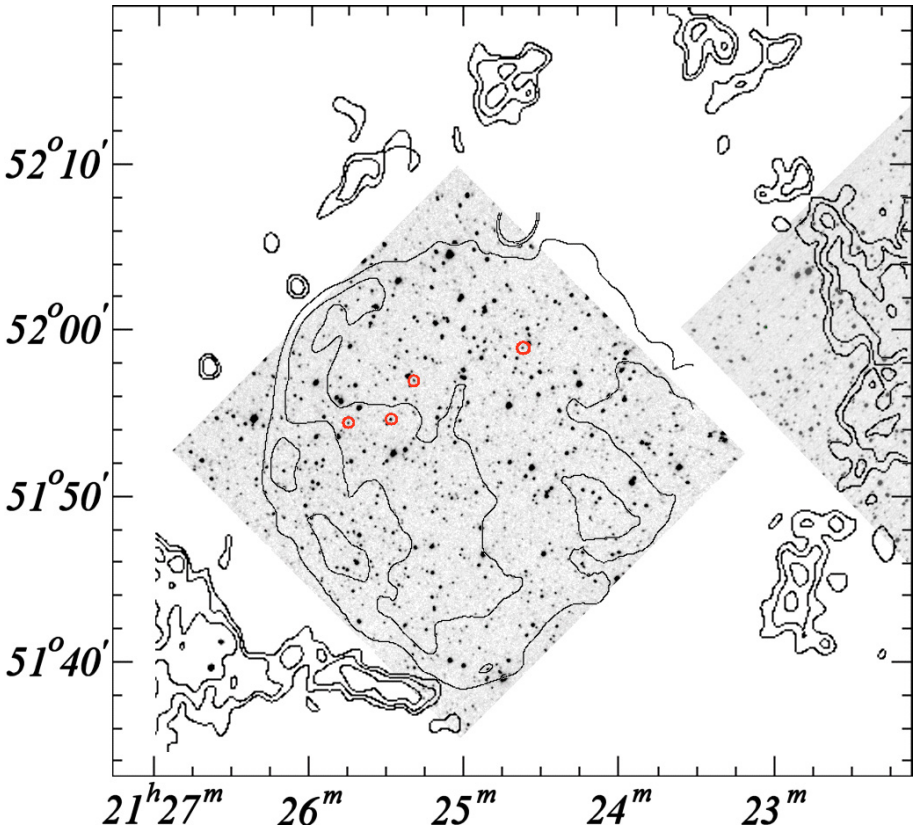

Fig. 8. A composite optical, radio continuum and H I line image, showing V-band optical images of the sky within the contoured H I line image of the stellar wind bubble. Each optical field of view is $0.5^\circ \times 0.5^\circ$ (that of the Devon Astronomical Observatory telescope). Only part of field 2 (upper right) overlaps the bubble, while field 1 is fully within it. The four stars identified as residents of the SWB (see Sect. 5) are circled. The three B0V stars are seen at left, while the O4V star is very nearly centred within the H I bubble. The continuum contours of 3C 434.1 are also drawn, showing the SNR's relation to the SWB and the stars responsible for its formation. Coordinates on axes are $(\alpha, \delta)(J2000)$.

Table 3. Eleven stars towards 3C 434.1 with observed reddenings that are consistent with that observed toward the SNR/SWB ($E(B-V)$ = 2.1 mag), i.e. 1.7 mag $\leq E(B-V) \leq$ 2.5 mag. The uncertainty in the assigned spectral type is on average plus or minus one sub-type (e.g. an O5 is O4-O6 within uncertainty). Distances are calculated using reddening law $R_V = A_V/E(B-V)$ = 3.1. All distances have an uncertainty of ±30%.

Star	$B-V$ (±13%)	$U-B$ (±20%)	m_V (±0.07 mag)	Assigned MK Type	M_V (±0.3 mag)	d (kpc) (±30%)	$E(B-V)$ (±0.23 mag)
1	1.45	0.06	14.95	B0	−4	5.1	1.74
2	1.75	0.11	13.55	O5	−5.7	3.7	2.08
3	1.72	0.44	13.92	B2	−2.47	1.2	1.95
4	1.46	0.02	15.05	B0	−4	5.2	1.77
5	1.62	0.40	14.10	B2	−2.47	1.0	1.84
6	1.66	0.21	14.04	B0	−3.9	2.4	1.95
7	1.86	−0.01	14.33	O4	−6.0	4.9	2.22
8	1.61	0.22	14.33	B1	−3.7	2.7	1.89
9	1.56	0.31	13.78	B2	−2.47	1.4	1.80
10	1.36	0.00	14.57	B0	−4	4.8	1.66
11	1.40	0.14	14.70	B1	−3.2	3.5	1.66

6. Conclusion

We have presented evidence that the H I environment near SNR 3C 434.1 has been shaped by a cluster of at least five stars, four of which are still affecting their surroundings, and the fifth of which produced the SNR itself. A thin walled H I shell surrounds the stars and the SNR (at a distance of 5.2 ± 1.1 kpc), and we confirm what its tattered appearance and low expansion velocity (14 km s^{-1}) suggest: it is an old stellar wind bubble which has hosted only 1 supernova event, and is now beginning

Table 4. Four stars from Table 3 with photometric distances and reddenings consistent with the SWB around 3C 434.1. Sources of the physical values v_∞, luminosity, mass and effective temperature are from Schaerer & de Koter (1997).

Star	Type (range)	α,δ (J2000)	v_∞ (km s^{-1})	$\log(L/L_\odot)$	M ($M_\odot$)	$T_{\rm eff}$ (K)	$\dot{M}/10^{-6}$ ($M_\odot$ yr^{-1})	$L_{\rm w}/10^{36}$ (erg s^{-1})	$\dot{M}_6 v_{2000}^2$
1	B0 (O9–B1)	$21^{\rm h}25^{\rm m}46.2^{\rm s}$ $51°54'52.5''$	2890	4.658	20	35 500	0.088	0.23	0.18
4	B0 (O9–B1)	$21^{\rm h}25^{\rm m}18.7^{\rm s}$ $51°57'29.2''$	2890	4.658	20	35 500	0.088	0.23	0.18
7	O4 (O3–O5)	$21^{\rm h}24^{\rm m}33.7^{\rm s}$ $51°59'19.4'$	3100	5.85	70	50 000	1.30	3.94	3.12
10	B0 (O9–B1)	$21^{\rm h}25^{\rm m}28.8^{\rm s}$ $51°54'59.3''$	2890	4.658	20	35 500	0.088	0.23	0.18

to dissipate in the ISM. Much of the shell is comprised of cool (80 K) H I gas, and it is concluded that the far end cap (seen as a dark area amidst a bright emission field) is absorbing emission from a warm uniform background of H I emission. We develop a geometric model of this bubble in three dimensions, and fit it to the bubble's appearance in velocity space.

Acknowledgements. The authors would like to thank Tom Landecker (DRAO) for his thoughtful comments on our manuscript. The Dominion Radio Astrophysical Observatory is operated as a national facility by the National Research Council of Canada. The Canadian Galactic Plane Survey is a Canadian project with international partners, and is supported by a grant from the Natural Sciences and Engineering Research Council of Canada (NSERC). This work has been supported by NSERC operating grants to T. Landecker, D. Routledge, D. Hube, and S. Morsink. T. Foster has been supported by an NSERC Graduate Scholarship.

References

Abbott, D. C. 1982, ApJ, 259, 282
Bessel, M. 1990, PASP, 102, 1181
Boyle, R. P., Dasgupta, A. K., Smriglio, F., Straizys, V., & Nandy, K. 1992, A&A, 95, 51
Cappa, C., Pineault, S., Arnal, E. M., & Cichowolski, S. 2002, A&A, 395, 955
Cazzolato, F., & Pineault, S. 2003, AJ, 125, 2050
Chiosi, C., Nasi, E., & Sreenivasan, S. R. 1978, A&A, 63, 103
Cox, A. N. 2000, Allen's Astrophysical Quantities, ed. A. N. Cox (New York: Springer-Verlag)
Foster, T., & Routledge, D. 2001, A&A, 367, 635 (Paper I)
Foster, T., Hube, D., Couch, J., et al. 1999, ASP Conf. Ser., 189, 111
Foster, T., & Routledge, D. 2003, ApJ, 598, in press
Garmany, C. D. 1994, PASP, 106, 25
Gathier, R., Pottasch, S. R., & Pel, J. W. 1986, A&A, 157, 171
Gibson, S. J., Taylor, A. R., Higgs, L. A., & Dewdney, P. E. 2000, ApJ, 540, 851
Higgs, L. A., & Tapping, K. F. 2000, AJ, 120, 2471
Høg, E., Fabricius, C., Makarov, V. V., et al. 2000, A&A, 355, 27
Koo, B-C., & McKee, C. F. 1992, ApJ, 388, 93
Kothes, R., Uyaniker, B., & Pineault, S. 2001, ApJ, 560, 236
Landecker, T. L., Dewdney, P. E., Burgess, T. A., et al. 2000, A&A, 145, 509
Mantovani, F., Nanni, M., Salter, C., & Tomasi, P. 1982, A&A, 105, 176
McKee, C. F., van Buren, D., & Lazareff, B. 1984, ApJ, 278, 115
Oja, T. 1996, BaltA, 5, 103
Panagia, N. 1973, AJ, 78, 92
Predehl, P., & Schmitt, J. H. M. M. 1995, A&A, 293, 889
Reich, W., Reich, P., & Fürst, E. 1997, A&A, 126, 413
Roberts, W. 1972, ApJ, 173, 259
Russeil, D. 2003, A&A, 397, 133
Saken, J. M., Shull, J. M., Garmany, C. D., Nichols-Bohlin, J., & Fesen, R. A. 1992, ApJ, 397, 537
Schaerer, D., & de Koter, A. 1997, A&A, 322, 598
Steigman, G., Strittmatter, P. A., & Williams, R. E. 1975, ApJ, 198, 575
Taylor, A. R., Gibson, S. J., Peracaula, M., et al. 2003, AJ, 125, 3145
Uyanıker, B., Kothes, R., & Brunt, C. M. 2002, ApJ, 565, 1022
Weaver, R., McCray, R., Castor, J., Shapiro, P., & Moore, R. 1977, ApJ, 218, 377